minerals

MDPI

Joint Inversion with Borehole and Semi-Airborne TEM Data Based on Equivalent Filament Approximation

Junjie Wu [1,2,*], Qingquan Zhi [1,2,*], Xiaohong Deng [1,2], Xingchun Wang [1,2] and Yi Yang [1,2]

1 Institute of Geophysical and Geochemical Exploration, Chinese Academy of Geological Sciences, Langfang 065000, China; dengxiaohong@mail.cgs.gov.cn (X.D.); wxingchun@mail.cgs.gov.cn (X.W.); yyi@mail.cgs.gov.cn (Y.Y.)
2 Laboratory of Geophysical EM Probing Technologies, Ministry of Natural Resources, Langfang 065000, China
* Correspondence: wjj498211@126.com (J.W.); zhiqingquan@gmail.com (Q.Z.)

Abstract: The borehole transient electromagnetic (TEM) method can be useful in deep mineral exploration to detect blind ore bodies beside or below the borehole, and is especially adapted to finding small-scale, deep, rich ore bodies. In this method a transmitting loop is deployed on the top surface of the Earth, while a receiving coil is moved down the borehole. As the borehole TEM method is limited by the borehole's location and depth, so its exploration scope is limited. The surface to airborne TEM method is a semi-airborne TEM configuration that transmits on the surface and receives TEM response in air. The two systems are combined into one system in this study, sharing the transmission loop deployed on the surface. With this combined system, the TEM response in the borehole and in the air can be observed at the same time. This paper employs a joint interpretation method based on the equivalent filament, which is introduced to obtain more reliable geometric information for the target with both borehole and aerial TEM data. The eddy currents induced in a thin confined conductor can be represented by equivalent current filaments, and the distribution of filaments can reflect the position and geometry of the conductor. Therefore, geometric parameters of targets can be obtained by filament inversion, and the joint inversion can be more accurate with both borehole and aerial response. Numerical modeling results show that the joint inversion based on the equivalent filament results can reliably obtain the geometric parameters of the thin conductive plate embedded in half space.

Keywords: TEM; borehole TEM; surface to airborne TEM; equivalent filament; joint inversion

1. Introduction

The borehole transient electromagnetic (TEM) method has become an important exploration method for conductive mineralization, particularly in areas where the ability of a surface electromagnetic (EM) method to define a target is limited either by significant depth or by interfering conductive bodies such as overburdened, shallow sulfides and peripheral mineralized horizons [1–3].

Borehole TEM usually refers to surface to borehole TEM, transmitting on the ground and receiving TEM response along the borehole. As the receiving probe is close to the targets, more reliable information on the deep ore bodies can be obtained than on the surface [4,5]. The receiving probe has the opportunity to detect the deep targets at close range and can gain useful geological information in the deep exploration [6–8].

However, due to the complexity of electromagnetic theory in relation to the borehole, it is difficult for the current data processing and interpretation methods to meet the current quantitative demand. Moreover, in the field of data interpretation and inference, single borehole information can only indicate the approximate location of the ore body near the borehole. It is difficult to provide more accurate geometric parameters for the target, which depends on drilling another borehole to carry out the next measurement.

Curve feature analysis methods, such as extreme point method and zero position method, are mainly used to provide the relative positions of target ore bodies [1,6]. The vector intersection method can only primarily indicate the approximate orientation of the target body center [9]. The 1D inversion and apparent resistivity interpretation methods are suitable for understanding the electrical distribution of background strata, which is not conducive to displaying local targets [10–14]. The equivalent current filaments method can roughly delineate the scope and central position of the target body [15–17], but at present, there needs to be equivalence in the inversion of borehole data to some extent, which is not accurate enough to reflect the information of the target bodies [18,19].

Surface to airborne TEM is a semi-airborne configuration, which transmits on the ground and receives in the air [20,21]. The aerial TEM response of the target body can be acquired quickly with a flight platform [22,23]. It has the advantages of high-power transmitting on the ground and fast scanning in the air. It has been a hot research method in recent years [24]. Many researchers have done a lot of research work in detection mode [25], surface to air transient electromagnetic system development [26–30], surface to air data processing [31,32] and applications in different fields [33,34].

For this reason, this paper presents a combined configuration of borehole TEM and surface to airborne TEM. By using the common ground source for the combined device, three-component transient responses in the borehole and the air can be observed separately and interpreted comprehensively. The two sets of data in the air and in the borehole complement each other and have higher resolution in both vertical and horizontal directions, so as to improve the reliability of interpretation. The results show that the eddy current generated by the excited conductor can be equivalent to a set of current loops [8]. The early current loops reflect the boundary of the anomalous body, while the late current loops mainly reflect the center of the anomalous body [35–37]. Therefore, the geometric shape of the target geological body can be obtained by inverting the geometric parameters of the equivalent current loop at different times.

We use the data from the test survey to illustrate our processing steps. We first introduce the principle objective of processing semi-AEM data in frequency domain. We first introduce the basic principle of the equivalent filament and the influence degree of the seven parameters of the filament. Then, we describe the details of the joint inversion method with semi aerial and borehole TEM. Data processing involves two main steps: (1) abnormal field extraction; and (2) joint inversion of anomaly field. The processing results are validated by comparison with joint inversion results with semi-airborne inversion or borehole data inversion alone. Deep mineral exploration has always been a difficult problem. The transient electromagnetic method is an important geophysical prospecting method for deep mineral exploration. In this study, a joint detection device of surface to borehole and surface to airborne TEM is proposed, and a fast interpretation method based on an equivalent current loop is introduced, in order to make these two configurations complement each other, and can obtain reliable data both vertically and horizontally, so as to interpret the deep ore body more reasonably.

2. Methodology

When the conductive plate model is located in a uniform primary field, if the current in the transmission loop is suddenly turned off and the primary field disappears instantaneously, according to Faraday's law, in order to maintain the original uniform magnetic field in the conductor, the eddy current is immediately induced in the plate, and the magnetic moment of the eddy current induced on the conductive thin plate is always perpendicular to the plate [35]. The induced eddy current will form a current ring distribution similar to the shape of the conductive plate in the plate. In the early stage, it is concentrated on the edge of the plate and then diffuses to the center of the conductor. After a short time interval, this current distribution reaches a quasi-equilibrium state, and then makes a simple amplitude attenuation. It can be proved by theory and numerical

simulation that this current distribution can be represented by an equivalent current loop not only in the late stage, but also in the early stage [1].

Similarly, if there is a conductive sphere in a uniform primary field, when the current in the emission loop is suddenly turned off, the sphere will immediately induce eddy current and only distribute on the surface of the sphere. Then, the distribution of the annular current in the sphere is dominated by the mutual influence of the magnetic field caused by these currents, moves into the sphere, and attenuates due to heat loss. Finally, the distribution of the current will not change with time. The current density near the center of the ball increases linearly along the distance of the radius, is relatively evenly distributed within one-half of the radius, and decreases slightly towards the edge of the ball. After that, the current and the corresponding external magnetic field begin to decay exponentially with a certain time constant until they disappear [36,37].

Under the excitation condition of magnetic source, the transient electromagnetic response above the surface (z < 0) can be equivalent through a simple current loop at any time after shutdown, as shown in Figure 1. Over time, the current ring diffuses downward and outward along an inclined cone [37]. Dyck proposed that multiple independent eigencurrents can be used to equivalent the eddy current of the thin plate, so as to calculate the transient electromagnetic field response of the conductive thin plate, and its feasibility is confirmed by numerical simulation [36].
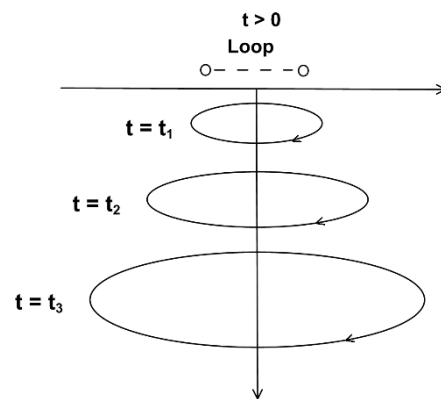

Figure 1. System of smoke rings [37].

According to the above theory, the eddy current generated by the excitation of the ore body can be equivalent to the field of the filament flowing in the ore body. The circular filament can well reflect the lenticular conductor.

The Cartesian coordinate system in free space is shown in Figure 2. The direction of the Z component is upward. The current loop is located in the X-Y plane and the center coincides with the origin of the coordinate. The radius is R and the current intensity is I. Then the expressions of the three components of the magnetic field produced by the current loop are as follows:

$$B_x = \frac{\mu IR}{4\pi} \int_0^{2\pi} \frac{z\cos\varphi}{r^3} d\varphi \tag{1}$$

$$B_y = \frac{\mu IR}{4\pi} \int_0^{2\pi} \frac{z\sin\varphi}{r^3} d\varphi \tag{2}$$

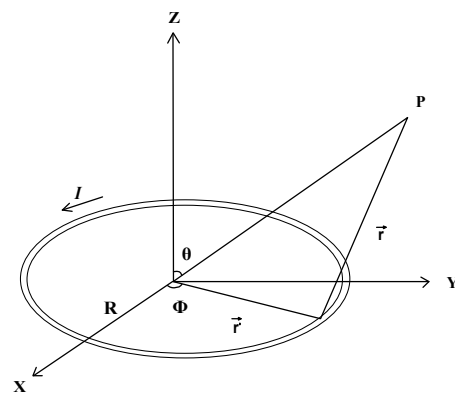$$B_z = \frac{\mu IR}{4\pi} \int_0^{2\pi} \frac{(R - y\sin\varphi - x\cos\varphi)}{r^3} d\varphi. \tag{3}$$

Figure 2. Current loop in free space.

There are seven parameters to describe the circular current loop model: center position (x, y, and z), radius, current value, dip angle, and azimuth.

In order to study the influence of each parameter on the current loop field, the seven parameters of the current loop were changed, and the rate of change of the current loop field after changing the parameters was calculated. The factor that measures the rate of change is:

$$\eta = \frac{\|\mathbf{B} - \mathbf{B_0}\|}{\|\mathbf{B_0}\|}, \tag{4}$$

whereas $\mathbf{B_0}$ is the initial current loop field matrix, $\mathbf{B}$ is the current loop field matrix after changing the parameters, and $\|*\|$ represents the two norms of the matrix. The significance of this factor is the ratio of the variation of the current loop field to the total modulus of the original current loop field after changing the parameters.

The model of the current loop is shown in Figure 3, where r = 100 m, I = 100 mA, $x = 0$, $y = 0$, $z = -100$, $\theta = 30°$, $\varphi = 0°$. The aerial survey line is $x = -100$–100 m, $y = 50$ m, $z = 10$ m, when the interval of points is 10 m. The borehole line is $x = 30$ m, $y = 50$ m, $z = 0$~200 m, when the interval of points is 10 m. The three-component magnetic field responses calculated on the basis of this parameter are shown in Figures 4 and 5.
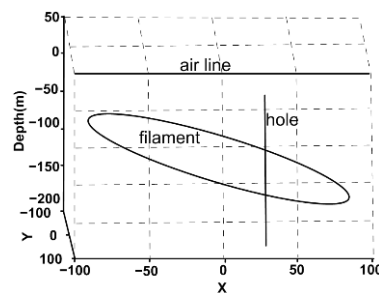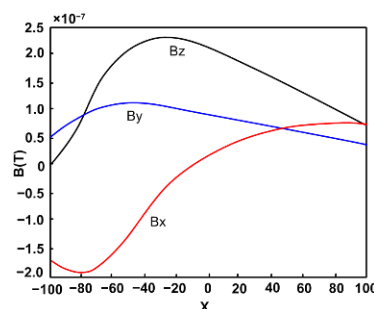

Figure 3. The filament model.
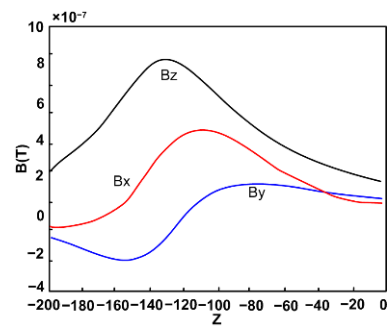

Figure 4. Aerial TEM response.

Figure 5. Borehole TEM response.

As can be seen from Figure 4, due to the tilt of the current loop, the maximum point of the vertical component and the zero point of the horizontal component in the air do not correspond to the central position of the current loop but shift to the opposite direction of the current loop. Figure 5 shows that the maximum point of the curve and the zero point of the horizontal component in the borehole migrate to the depth due to the downward inclination of the current loop.

3. Joint Inversion

The joint inversion method of semi-airborne and borehole TEM data based on filament uses the pure anomaly field to locate the anomaly body. Therefore, it is necessary to extract the pure anomaly field first, and then carry out the joint inversion of the pure anomaly field. The general joint inversion scheme of semi-airborne and borehole TEM data is as follows:

Abnormal field extraction. Through the rough fitting of all data with a simple model, the background model is obtained, and the background field is subtracted from the total field to obtain the pure anomaly fields generated by the anomaly body;

Joint inversion of anomaly field. The objective function including both air and borehole pure anomaly response is constructed, and the appropriate optimization method is selected for joint inversion; The specific implementation process is described in detail below.

3.1. Anomaly Field Extraction

The interpretation method based on equivalent filament determines the geometric parameters of an anomalous body in free space, so it is necessary to extract the anomalous field and eliminate the influence of the background field.

The transmitter of borehole and surface to airborne TEM was fixed on the surface, and the coupling relationship between them and the underground media remained unchanged. The response of the secondary field at different positions was observed in boreholes and in the air. For homogeneous half-space and 1D models, the transient response observed in boreholes and in the air was continuous, and there was no sudden change.

When a conductor exists underground, the anomalous field is generated and superimposed on the background field. Because the influence range of anomalous response is limited, the approximate 1D electrical distribution in the observation area can be obtained by fitting the data in a larger spatial range. Using this 1D electrical distribution as the approximate background model of the observation area, with the field generated by the background model as the approximate background field, the anomalous field data can be obtained approximately by making a difference between the total field data and the approximate background field data.

In 1D forward fitting, the objective function is as follows:

$$\varphi = \frac{\|V_s^{obs} - V_s^{fit}\|}{\|V_s^{obs}\|} + \frac{\|V_b^{obs} - V_b^{fit}\|}{\|V_b^{obs}\|}. \tag{5}$$

Here, *V* represents normalized attenuation voltage, superscript ***obs*** and ***fit*** represent observation value and fitting value respectively, and subscripts ***s*** and ***b*** represent the field

value of aerial and borehole lines respectively. For a large-space range, the background field in the observation range can be approximately obtained by minimizing Equation (5).

3.2. Joint Inversion Objective Function of Anomaly Field

Considering that there was no difference of magnitude in the variation of field caused by various parameters, it was unnecessary to introduce a correction term in the construction of the objective function. With the view of best fitting observation data, the objective function was selected as the relative difference between observation data and fitting data. In addition, taking into consideration the suppressing of normal distribution interference and balancing the weight of each data, the least square objective function was selected:

$$
\begin{aligned}
\varphi &= r_g^T C_{mg} r_g + r_b^T C_{mb} r_b \\
r_g &= \frac{d_g^{obs} - d_g^{fit}}{d_g^{obs}}, r_b = \frac{d_b^{obs} - d_b^{fit}}{d_b^{obs}} \\
d_g &= \left(B_{xg} B_{yg} B_{zg} \right), d_b = \left(B_{xb} B_{yb} B_{zb} \right)
\end{aligned}
\tag{6}
$$

where the subscripts g and b represent the air and borehole components, respectively, B represents the magnetic field component generated by the current filament, and C is the variance matrix of the data.

In order to ensure the steady decline of the objective function, the feasible direction method was adopted when minimizing the objective function. Feasible direction method is a method to solve the optimization problem. The search direction adopted in the iterative process is feasible direction, the generated iteration point is always within the feasible region, and the value of the objective function decreases monotonously. The specific iterative steps were as follows:

(1) Give an initial point $x^0 \in D$, allow error $\varepsilon > 0$, iterations number $k = 0$;

(2) Solve the linear programming problems $\min_{x \in D} \nabla f(x^k)^T x$, get the optimal solution $y^k \in D$;

(3) If $\left| \nabla f(x^k)^T (y^k - x^k) \right| \leq \varepsilon$, then the optimal solution is considered to have been found, stop the iteration, and select the estimated solution $x^* \approx x^k$, otherwise, go to step 4;

(4) Obtain the optimal step size factor by one-dimensional search $\min_{0 \leq \lambda \leq 1} f(x^k + \lambda(y^k - x^k))$, get the optimal step λ^k, set $x^{k+1} \approx x^k + \lambda^k(y^k - x^k)$, number of iterations $k = k + 1$, go to step 2.

B_x, B_y and B_z in the fitting data are calculated by Equations (1)–(3), respectively. Through inversion, seven parameters of the equivalent current loop can be obtained, including: center position (x, y, and z), radius, current value, dip angle, and azimuth.

4. Numerical Modeling

In order to verify the validity of the joint interpretation method, we carried out numerical simulations. The inversion method based on equivalent filament approximation is suitable for the case of high contrast of conductivity and ore body have a size which is similar in its depth. The borehole and air measurements can control the horizontal and vertical parameters of ore bodies better respectively. The target geological body of TEM exploration is usually a high conductive body, which is obviously different from the surrounding rock in electrical properties. Therefore, high conductive thin plates with different dip angles and depths in half space were selected for the model.

4.1. Horizontal Conductive Thin Plate Embedded in Half Space

The model was a horizontal high conductive thin plate in half space. In the forward calculation, the emission waveform is step wave, the ramp time is 0, and the current is 1A. The position of plate, loop, borehole, and survey points are shown in Figure 6. The loop size is 1000 m × 1000 m; center coordinates are 0, 0; the length of the survey line is 800 m; line interval is 100 m; station interval is 50 m; survey points range from −400 to 400.

The resistivity of half space is 1000 $\Omega \cdot$m. The parameters of the conductive thin plate are as follows: $\sigma = 50$ S, $\theta = 0°$, $\varphi = 0°$; size is 300 m $\times$ 300 m; center coordinates are $x = 0$ m, $y = 0$ m, $z = -150$ m. The plane coordinates of the borehole are $x = 100$ m, $y = 50$ m, and time channels are shown in Table 1. The numerical simulation is mainly calculated by Maxwell software.

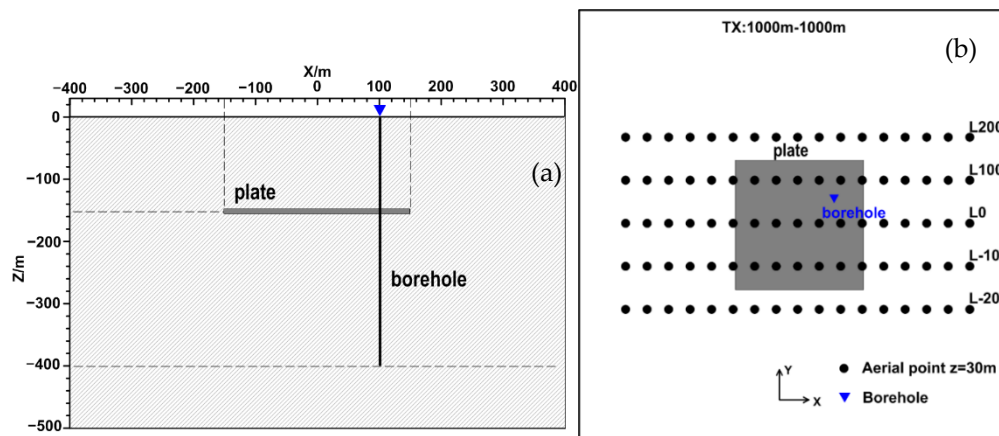**Figure 6.** The diagram of design model, transmit loop and station. (**a**) front view, (**b**) top view.

Table 1. TEM time channels.

Chn	t/ms	Chn	t/ms	Chn	t/ms	Chn	t/ms
1	0.0865	8	0.293	15	0.991	22	3.336
2	0.105	9	0.35	16	1.178	23	3.965
3	0.123	10	0.415	17	1.401	24	4.715
4	0.145	11	0.494	18	1.666	25	5.608
5	0.174	12	0.588	19	1.981	26	6.670
6	0.208	13	0.701	20	2.357	27	7.932
7	0.246	14	0.833	21	2.804	28	9.435

TEM response plots of three components in the borehole are given in Figure 7. It can be seen in the figure that the shape and amplitude of the three component curves are different. Figure 8 shows the inversion results using only three-component transient response data for the borehole. The results are presented from different perspectives. It can be seen that the current loop obtained by inversion is horizontal, and the depth and plane range are basically consistent with the model.
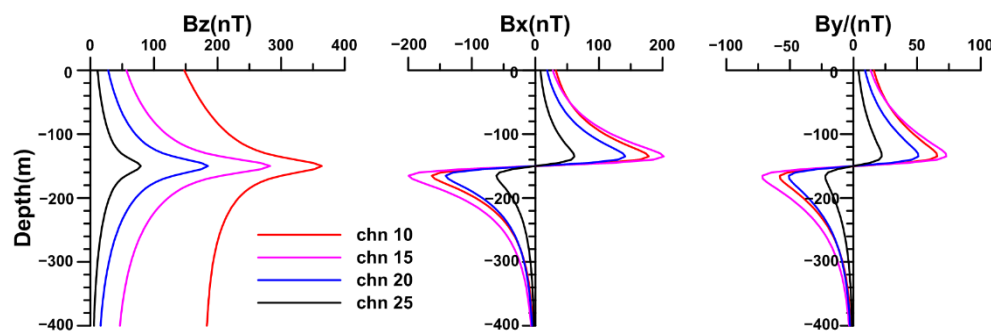

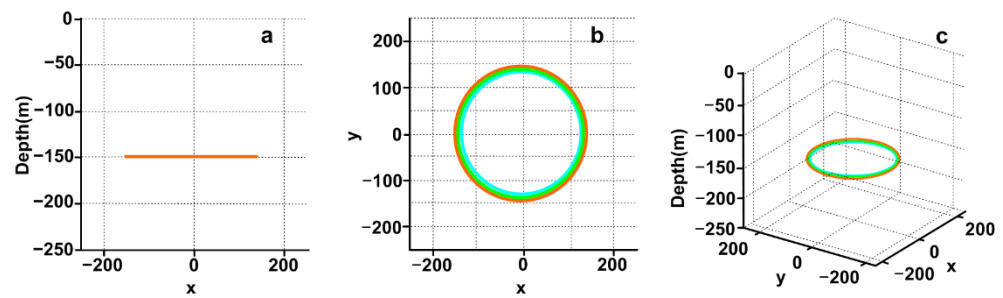**Figure 7.** Three component transient response plot curves in borehole.

Figure 8. Inversion results with borehole three-component TEM data. (**a**) Side view, (**b**) Top view, (**c**) Perspective view.

Table 2 shows the comparison of current loop parameters retrieved from different time channels (number 10, 15, 20, and 25). It can be seen from the table that the inversion parameters are basically consistent with the theoretical model. The z coordinate and dip angle of the current loop center are more accurate than other parameters, and the deviation of x and y coordinate parameters reaches 1–6 m.

Table 2. Inversion results with borehole TEM data.

Channel	r (m)	I (mA)	x (m)	y (m)	z (m)	θ (°)	φ (°)	Fit Error %
10	143.34	119.92	−6.14	2.50	−150.01		0	1.57
15	139.31	80.07	−6.30	2.06	−150.09	0.18	0	1.54
20	135.56	31.18	−6.63	1.39	−150.07	0.26	359.53	1.49
25	133.93	3.26	−6.90	0.98	−150.10		0.00	1.47
Initial value	100	100	100	100	−100	0	0	0

Figures 9–11 show three component TEM plot curves (channel 10, 15, 20 and 25) of three survey lines L0, L100 and L200 in the air. L0 is the main survey line and passes through the center of the transmitting loop, so the Y component response is zero. On the whole, the Z component is positive anomaly, the amplitude of the main survey line is the strongest, and the amplitude of the survey lines on both sides gradually weakens. X component takes point 0 as the center, the positive and negative are symmetrical, and the positive and negative peaks correspond to the two boundaries of the anomaly body. As the positive and negative amplitudes are the same, which reflects that the target body is horizontal, and the zero point corresponds to the anomaly center. The abnormal center of the Y component corresponds to the center of the target body, and the positive and negative are mainly affected by the coordinate position.
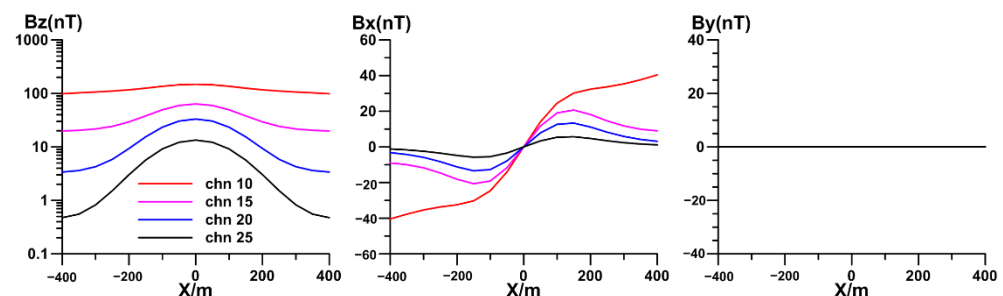

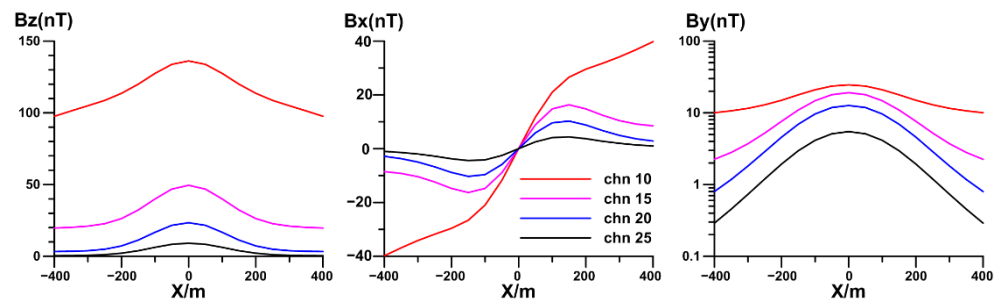**Figure 9.** Three component TEM response plot curves of L0.

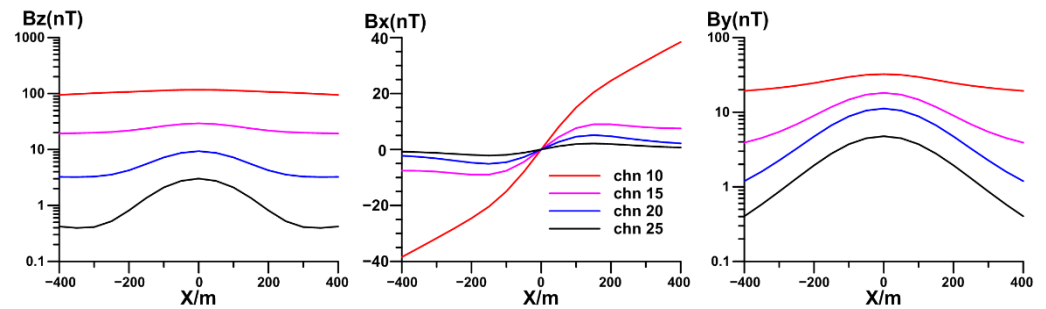**Figure 10.** Three component TEM response plot curves of L100.

Figure 11. Three component TEM response plot curves of L200.

Figure 12 shows the inversion results of L0, L100 and L200 using aerial data only for three components. It can be seen that the result of L0 is relatively accurate, the depth of inversion results of different time channels are consistent with the theoretical value, and the early time channel inversion results of L100 and L200 line are in agreement with each other in depth, but the current filament of middle and late channel gradually shrinks and the depth becomes deeper. It is mainly affected by the equivalence of magnetic moment.
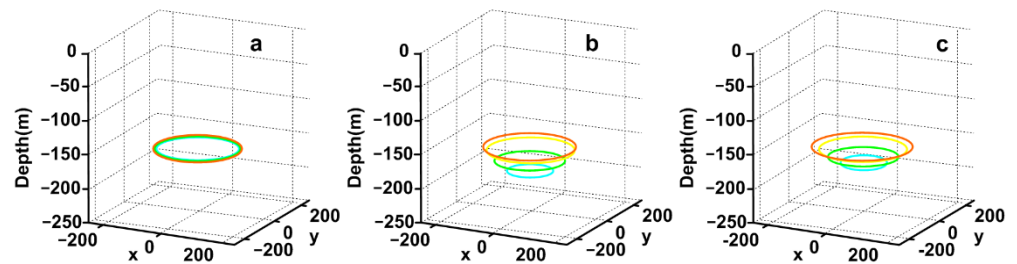
Figure 12. Inversion results of aerial lines data (**a**) L0, (**b**) L100, (**c**) L200.

Table 3 gives the comparison inversion filaments parameters of three lines with different time channels (number 10, 15, 20, and 25). As can be seen from the table, the fitting errors of the inversion results are no more than 5% on the whole, which is approximately consistent with the theoretical model. However, according to the analysis of different parameters, r and z coordinate errors are relatively larger and x, y, and φ are more accurate. It can be seen that the inversion results of aerial data are relatively accurate in transverse control of the plane position range of the abnormal body, while relatively larger in longitudinal control of the depth.

Table 3. Inversion results with aerial TEM data.

Line	Chn	r (m)	I (mA)	x (m)	y (m)	z (m)	θ (°)	φ (°)	Fit Error %
L0	10	131.4	140.64	−6.14	0.00	−157.04	0.00	0.00	0.24
L0	15	126.2	96.08	−6.30	0.00	−157.50	0.01	0.00	0.22
L0	20	120.9	38.62	−6.63	0.00	−158.08	0.01	0.00	0.22
L0	25	118.1	4.13	−6.90	0.00	−158.47	0.01	0.00	0.22
L100	10	165.14	71.39	0.57	−2.17	−118.25	3.62	0.55	4.28
L100	15	131.62	92.99	0.02	−0.77	−159.62	2.14	0.01	0.85
L100	20	111.04	48.83	−0.20	3.48	−169.57	2.14	0.00	1.69
L100	25	91.99	7.87	−0.48	−0.66	−179.77	2.21	0.31	2.37
L200	10	150.88	114.64	−0.09	−8.33	−153.76	0.37	0.00	1.23
L200	15	136.58	89.48	−0.11	−7.24	−158.60	0.43	0.00	1.37
L200	20	104.58	55.96	−0.24	0.26	−168.97	0.42	0.00	1.77
L200	25	69.73	13.47	−0.09	1.53	−177.74	6.55	0.00	2.26
initial value		100	100	100	100	−100	0	0	

Figure 13 shows the joint inversion results with both borehole and aerial TEM data. It can be seen that the inversion result is close to the theoretical model both in depth and in plane position. Table 4 shows the comparison of inversion parameters under different conditions. As can be seen from the table, the inversion results of different survey lines and channels are relatively consistent, and the parameters are in good agreement with the theoretical model. The parameters of *x*, *y*, *z*, radius, and azimuth of the central point of the current filament are more accurate than those obtained in the air or in the hole only.
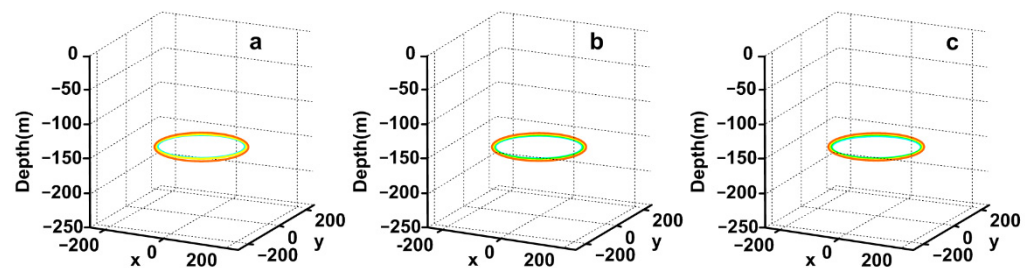

Figure 13. Joint inversion results with borehole and aerial TEM data. (**a**) L0, (**b**) L100, (**c**) L200.

Table 4. Joint inversion results with borehole and aerial TEM data.

Line	Chn	r (m)	I (mA)	X (m)	Y (m)	Z (m)	θ (°)	φ (°)	Fit Error %
L0	10	138.28	121.49	−1.60	2.62	−148.52	3.75	1.02	3.89
L0	15	133.60	81.79	−1.60	2.48	−148.54	0.00	1.06	3.91
L0	20	129.10	32.15	−1.60	2.15	−148.67	0.10	1.07	3.98
L0	25	126.83	3.39	−1.60	1.98	−148.70	0.08	1.10	4.05
L100	10	139.06	119.40	−1.32	3.09	−149.71	1.54	0.00	3.97
L100	15	135.07	79.90	−1.50	2.57	−149.74	1.21	0.00	3.89
L100	20	131.37	31.17	−1.77	1.89	−149.79	0.85	0.04	3.88
L100	25	129.68	3.27	−1.91	1.46	−149.74	0.37	0.18	3.92
L200	10	140.65	117.81	−2.13	3.56	−149.95	9.07	0.00	5.18
L200	15	136.5	78.84	−2.29	2.88	−149.88	8.81	0.00	5.03
L200	20	132.48	30.95	−2.54	1.71	−149.45	8.07	0.34	4.92
L200	25	130.44	3.26	−2.69	1.15	−149.2	4.66	0.56	4.87
Initial value		100	100	100	100	−100	0	0	

Considering that there is a certain degree of noise in the field measured data, in order to test the applicability of the inversion algorithm under the condition of noise, different levels of noise (10%, 20%, 40%) are added to the theoretical data of aerial L100 survey line and borehole, and the synthesized data are used for direct inversion. Inversion uses both borehole data and aerial data for joint inversion.

Table 5 shows the seven parameters of filament and fitting errors obtained by the inversion of different time channels under different noise levels. The results show that the fitting error of the inversion results is less than 6.08% when 10% noise is added. When the noise level reaches 20%, the fitting error is about 10%, and the fitting error is about 20% as the noise reaches 40%.

Table 5. Joint inversion results with borehole and aerial TEM data with different noise level.

Noise	Chn	r (m)	I (mA)	x (m)	y (m)	z (m)	θ (°)	φ (°)	Fit Error %
10%	10	141.52	118.34	−2.73	0.77	−149.32	1.85	0	6.03
10%	15	136.24	79.72	−1.96	1.34	−149.49	1.60	0	6.08
10%	20	132.13	31.42	−1.95	0.52	−150.03	1.26	0.53	4.91
10%	25	128.04	3.37	−2.54	0.40	−148.79	0.13	0.71	5.63
20%	10	139.67	121.21	−4.86	0.60	−148.52	0.05	1.56	9.29
20%	15	141.12	76.78	−3.86	−1.12	−149.09	0	2.07	12.06
20%	20	126.54	33.61	−3.63	0.62	−148.05	0	2.77	10.78
20%	25	136.06	3.11	−4.21	−4.46	−148.67	1.33	3.16	10.22
40%	10	152.45	111.01	−6.96	−11.2	−147.15	1.23	2.35	17.60
40%	15	126.65	82.64	2.26	1.12	−152.02	180.0	1.40	21.04
40%	20	131.18	32.60	−8.27	5.42	−148.97	90.90	4.17	20.28
40%	25	135.40	3.00	−3.58	2.35	−151.16	179.4	0	22.04
Initial value		100	100	100	100	−100	0	0	

Figures 14–16 show the comparison results of synthetic data and fitting data with 10%, 20% and 40% noise added to the theoretical data respectively. It can be seen that after adding different levels of noise, the inversion curve fit well with the synthetic curve, which can reflect the characteristics of the three component curves. Figure 17 is the joint inversion result after adding noise. It can be seen that, with the increase of noise level, there is a certain error in the geometric parameters of the retrieved filaments. The comparison results show that after adding noise to the synthetic data, the fitting error increases gradually with the improvement of noise level, but the inversion results are still within the acceptable range, which proves the stability of this approximation algorithm.
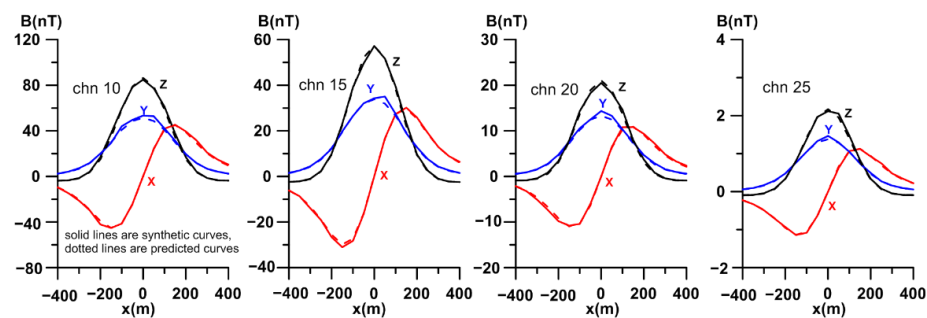

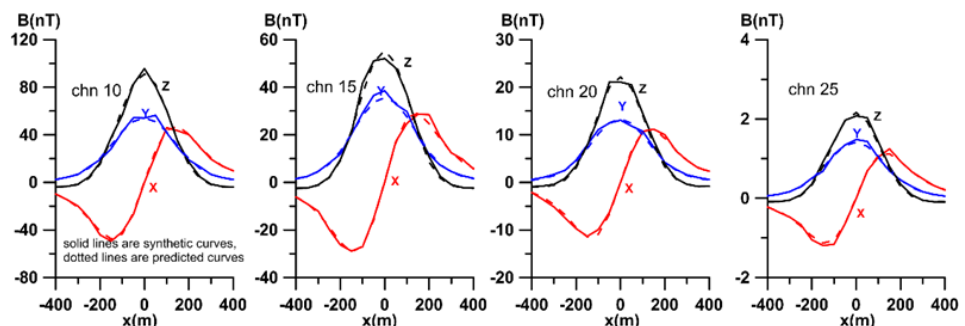**Figure 14.** Comparison of synthetic curves and predicted curves of L100 (10% noise).

Figure 15. Comparison of synthetic curves and predicted curves of L100 (20% noise).
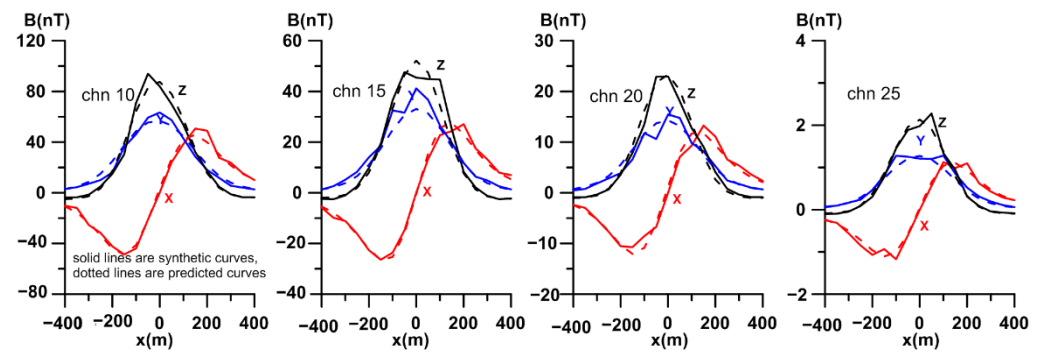
Figure 16. Comparison of synthetic curves and predicted curves of L100 (40% noise).
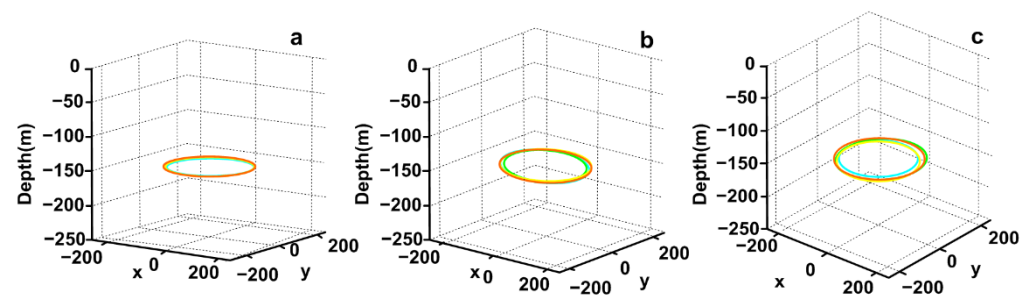

Figure 17. Joint inversion results with borehole and aerial TEM data. (**a**) 10% noise, (**b**) 20% noise, (**c**) 40% noise.

4.2. Inclined Conductive Thin Plate Embedded in Half Space

The model is an inclined high conductive thin plate embedded in half space. The position of plate, transmission loop, and station is shown in Figure 18.
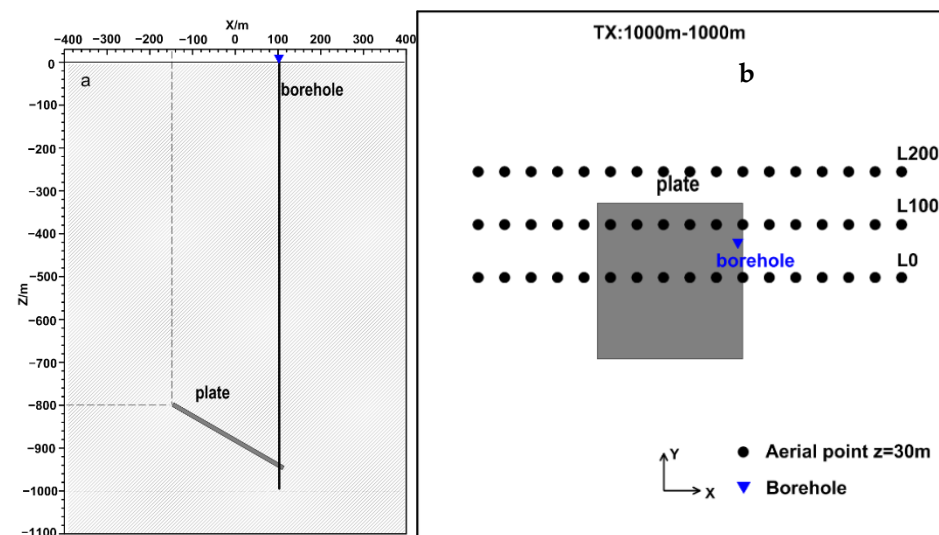

Figure 18. The diagram of design model, transmission loop and station. (**a**) Front view, (**b**) Top view.

In the forward calculation, the emission waveform is step wave, the ramp time is 0, and the current is 1A. The loop size is 1000 m × 1000 m; center point coordinates are 0, 0; length survey line is 800 m; interval of lines is 100 m; interval of stations is 50 m; stations range from −400 to 400. The resistivity of half space is 1000 Ω m, σ = 50 S, φ = 0°, θ = 30°; size of plate is 300 m × 300 m; plate center coordinate is 0 m, 0 m, −870 m; the hole plane coordinates are 100 and 50; time channels are shown in Table 1.

Figure 19 shows TEM response plots of three components in the borehole. The borehole passes through the edge of the conductive plate, the response of Z component is positive anomaly, and the X and Y components are anti-s anomaly, and cross the zero point at -940 m.
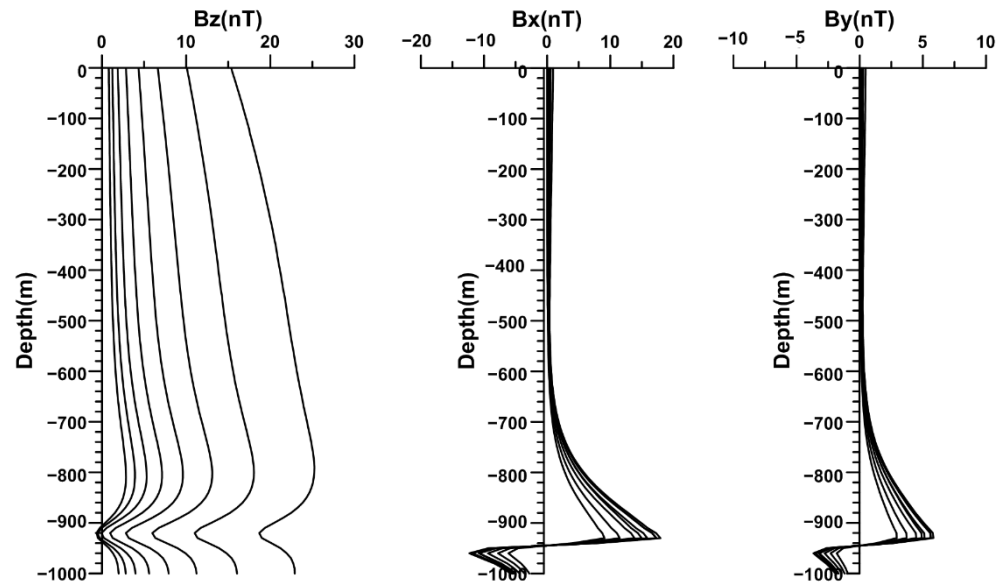

Figure 19. Three component transient response plot curves in borehole.

Figure 20 shows the inversion results with a three-component TEM response along the borehole. The spatial shape of a group of filaments are shown from different perspectives. In Table 6, the inversion current loop parameters from the borehole data with different time channels are listed. The detailed data of current loop parameters obtained from different time channels of borehole data are shown in Table 6. As can be seen from the table, the fitting errors of the inversion results are no more than 1% on the whole, which is consistent with the designed model. However, according to the analysis of different parameters, the values of z, φ, and θ are close to the theoretical values, while r deviates from the theoretical value.
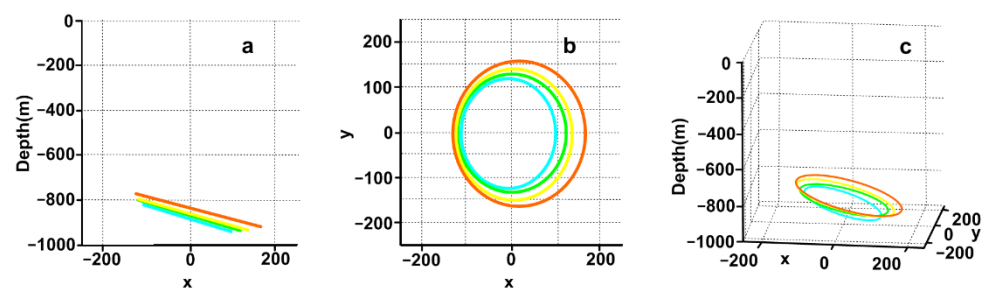

Figure 20. Inversion results with borehole three-component TEM data. (**a**) Front view, (**b**) Top view, (**c**) Perspective view.

Table 6. Inversion results with borehole TEM data.

Channel	r (m)	I (mA)	x (m)	y (m)	z (m)	θ (°)	φ (°)	Fit Error %
10	137.29	18.79	-1.67	-0.33	-877.69	29.68	0	0.14
15	128.48	13.84	-4.17	-0.11	-881.65	29.96	0	0.06
20	123.32	5.51	-4.30	-0.12	-881.67	29.95	0	0.06
25	120.29	0.59	-4.59	-0.12	-882.08	30.04	0	0.06

Figures 21–23 show the three component response curves of three survey lines in the air. It can be seen that the morphological characteristics of survey lines at different positions are basically the same, which is mainly related to the device and background field, and there is basically no abnormal display. In addition, from the transient response curves in the well and in the air, the deep data in the well show more obvious anomalies because they are closer to the abnormal body.
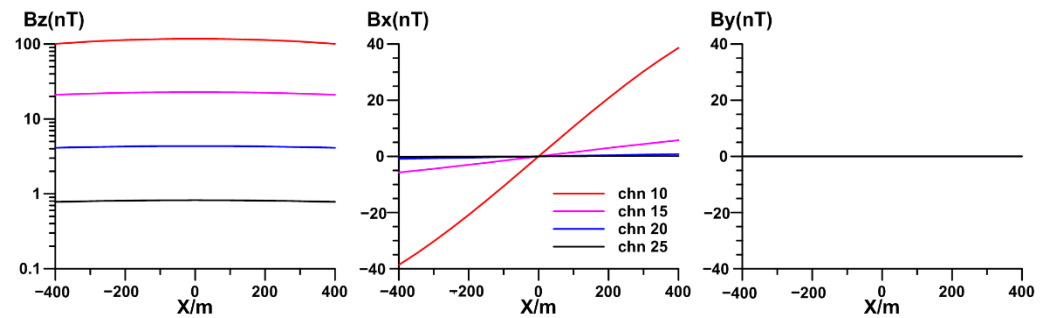

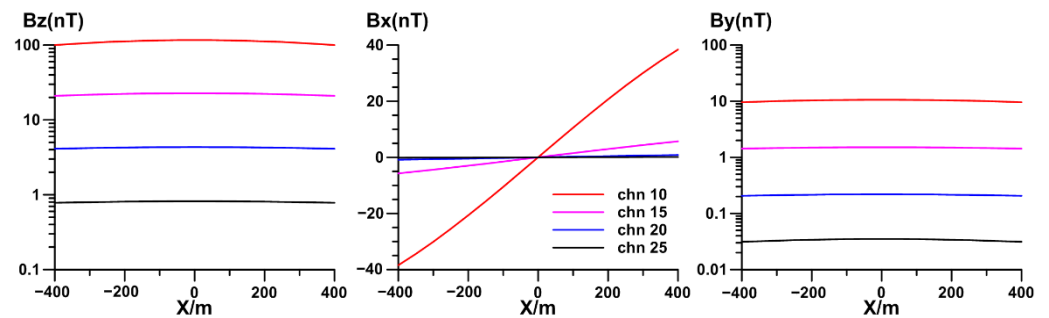**Figure 21.** Three component TEM response plot curves of L10.

Figure 22. Three component TEM response plot curves of L100.
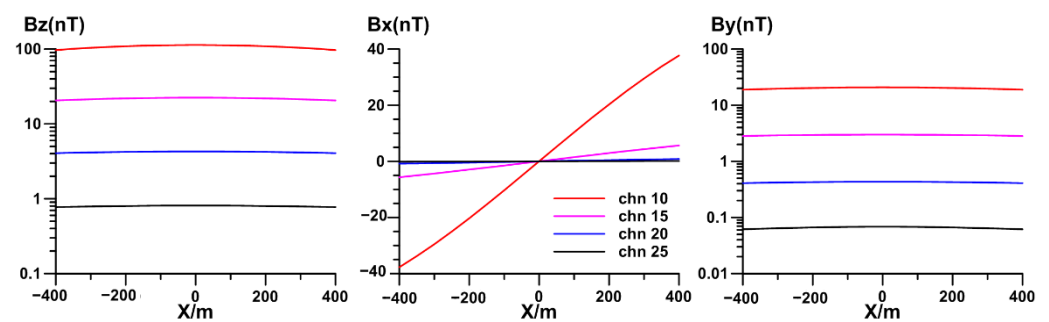

Figure 23. Three component TEM response plot curves of L200.

Figure 24 shows the inversion results of air lines L0, L100, and L200. It can be seen that the inversion results of aerial data are relatively accurate in transverse control of the plane position range of the abnormal body, and relatively large in the longitudinal control of the depth.

As can be seen from Table 7, the fitting errors of the inversion results are less than 2% on the whole. However, according to the analysis of specific parameters, the results of θ are approximate, while the errors from x, y coordinates, and the r individual time channel are relatively larger, which are mainly affected by the large, buried depth and weak response of the abnormal body.
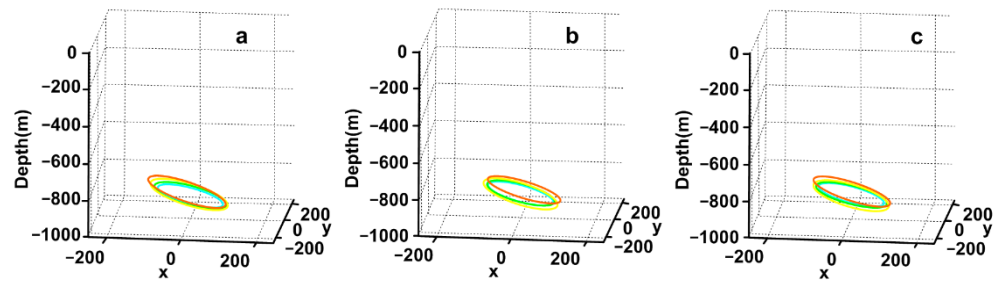
Figure 24. Inversion results with aerial TEM data. (**a**) L0, (**b**) L100, (**c**) L200.

Table 7. The inversion current filament parameters of survey lines in the air.

Line	Chn	r (m)	I (mA)	x (m)	y (m)	z (m)	θ (°)	φ (°)	Fit Error %
L0	0.415	66.01	78.73	0.82	26.69	−874.53	27.97	8.66	0.61
L0	0.991	53.27	77.46	−5.11	0.24	−879.67	28.87	0	0.17
L0	2.357	33.81	69.41	−1.04	0.21	−876.64	27.75	0.07	0.24
L0	5.608	11.89	52.73	21.09	0.83	−860.84	21.82	0.31	0.59
L100	0.415	111.54	27.84	6.41	51.99	−874.63	29.27	17.02	1.25
L100	0.991	110	18.11	−2.02	4.77	−874.53	29.42	1.17	0.14
L100	2.357	104.44	7.42	−1.71	4.49	−876.59	29.33	1.37	0.08
L100	5.608	96.61	0.88	−1.95	3.65	−876.94	29.27	1.09	0.09
L200	0.415	120.88	23.49	−2.03	54.85	−874.1	30.99	0.37	1.4
L200	0.991	113.55	17.06	−0.75	1.06	−875.04	29.36	0.43	0.1
L200	2.357	108.35	6.89	−1.02	1.07	−875.82	29.34	0.42	0.07
L200	5.608	93.58	0.94	−2.73	1.58	−877.21	29.39	5	0.09
initial value		100	10	100	100	−800	0	0	

Figure 25 shows the joint inversion results with both borehole and aerial TEM data. It can be seen that the inversion results are in agreement with the theoretical model both in depth and in plane positions. Table 8 shows the comparison of inversion parameters with different lines and channels. As can be seen from the detailed data, the inversion results of different survey lines and time channels are relatively consistent, and the inversion parameters are in agreement with the theoretical model. The parameters of x, y, z, r, and θ from joint inversion are more accurate than those from inversion with borehole or aerial TEM data only.
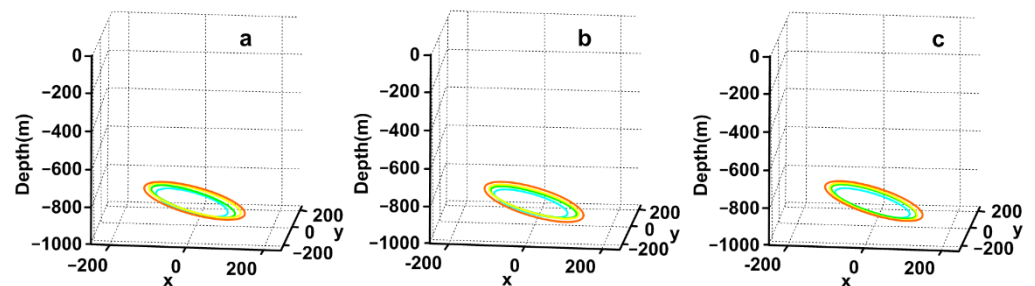

Figure 25. The inversion result of joint hole and survey line in the air. (**a**) L0, (**b**) L100, (**c**) L200.

The calculation results show that the joint inversion of borehole and air data can make up for the deficiency of single inversion using borehole or aerial data, so that reliable inversion results can be obtained both horizontally and vertically.

Table 8. Joint inversion results with borehole and aerial TEM data.

Line	Chn	r (m)	I (mA)	x (m)	y (m)	z (m)	θ (°)	φ (°)	Fit Error %
L0	10	147.02	16.04	3.05	−0.20	−870.91	29.14	0.00	0.94
L0	15	133.85	12.43	−1.06	−0.24	−876.92	29.71	0.00	0.32
L0	20	127.34	5.06	−1.76	−0.19	−877.94	29.77	0.00	0.29
L0	25	110.94	0.69	−7.46	0.84	−885.20	30.40	0.46	0.95
L100	10	147.02	16.04	3.05	−0.20	−870.91	29.14	0.00	0.94
L100	15	133.85	12.43	−1.06	−0.24	−876.92	29.71	0.00	0.32
L100	20	127.34	5.06	−1.76	−0.19	−877.94	29.77	0.00	0.29
L100	25	110.94	0.69	−7.46	0.84	−885.20	30.40	0.46	0.95
L200	10	147.24	16.03	1.76	−1.67	−870.32	29.18	0.00	1.26
L200	15	131.87	12.85	−2.03	−0.18	−878.04	29.83	0.00	0.28
L200	20	127.71	5.03	−1.58	−0.20	−877.80	29.77	0.00	0.28
L200	25	113.19	0.66	−6.86	0.43	−883.83	30.31	0.30	0.82
initial value		100	10	100	100	−800	0	0	

5. Discussion

5.1. Perturbation of Local Minimum during Inversion

Figure 26 shows the curves of the field value change rate caused by the change of filament parameters, which indicates the comparison between borehole and surface to airborne configuration. It can be seen that the variation characteristics of the field caused by the radius, current, x, y, and dip angle of the filament are monotonic functions, and the variation rate of the field caused by z and dip angle is non-monotonic. With the parameters of x, y, dip angle, and azimuth, the variation rate in the borehole is greater than that in the air, and the variation characteristics of the field caused by the electric current are the same in the air and in the borehole, while the variation rate of z in the air is greater than that in the borehole.
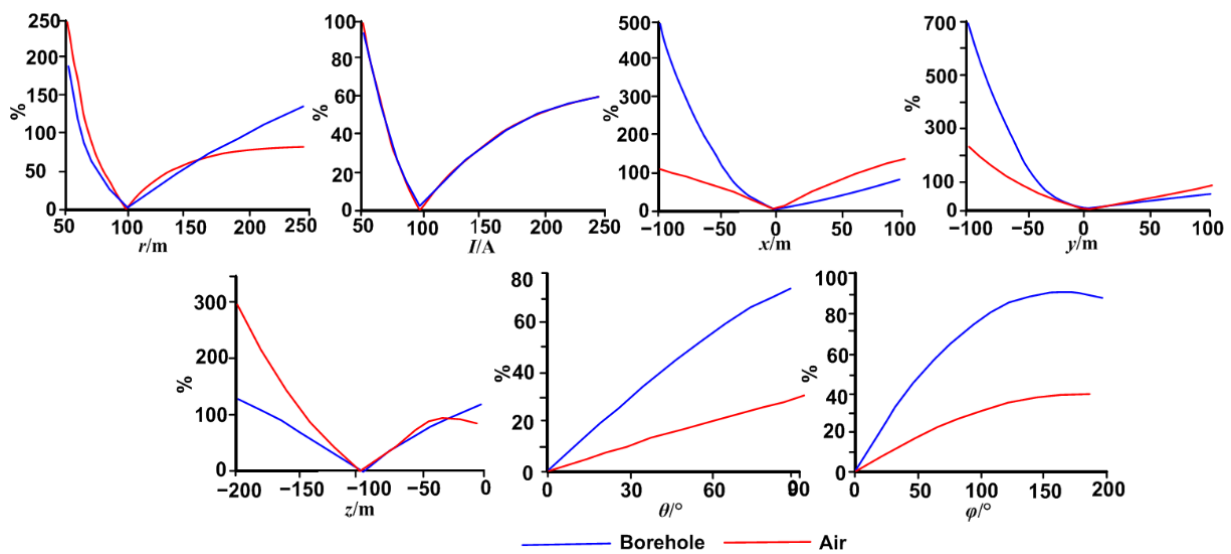

Figure 26. Curves of the variation rate of field value with 7 parameters.

It can be seen that the aerial data are more sensitive to the vertical position of the filament, while the borehole data are more sensitive to the horizontal position, the azimuth and dip angle of the filament. Considering that there is no magnitude difference in the field changes caused by the change of parameters, it was not necessary to introduce a correction term in the construction of the objective function, but the non-monotonic characteristics of the change of azimuth and z should be taken into account.

When it is determined that the inversion process falls into a local minimum, through some intervention strategies, the auxiliary inversion algorithm jumps out of the local minimum and realizes the global optimization.

The previous analysis shows that the change of the field is non-monotonic when the azimuth and z parameters are changing. In the process of minimization, the azimuth and z positions may fall into the local minimum, and the fitting difference is very large, but it cannot continue to decline with iteration. At this point, even if the iterative process continues, the global minimum cannot be reached. Additional perturbations are necessary to jump out of the local minimum and reach the global minimum in other correction directions.

The perturbation process is actually a form of interference for the iterative process. The perturbation process can be introduced only when the local minimum is determined to a large extent, to avoid meaningless perturbation, which is damaging for the normal correction process and wastes computing time. When the data fitting is of good quality, the fitting error is generally below 10%. We judged that the iteration had fallen into local minimum when the overall fitting difference was greater than 20% and could not decline with iterating but introduced perturbation. If the tendency of the current is less than $180°$, it is changed to $270°$, otherwise it is changed to $90°$, and if the distance between the filament z position and the measure point is less than the radius of the filament, then z is taken as $-2a$, otherwise, z is set as 0.

According to the previous discussion, there is generally only one local minimum point caused by φ and z, so the global minimum can be achieved by continuing iteration after perturbation.

5.2. Conductive Body Is Located below the Depth of the Borehole

In practical work, it is often necessary to carry out transient electromagnetic measurement in the borehole to determine whether there is a possibility of ore discovery in the deep. The revised version attempts to use the current loop model to discuss the joint inversion method in this case.

The design parameters are as follows: the radius of the current loop is 100 m, the current is 100 mA, and the coordinates of the center point are $(0, 0, -600 \text{ m})$, the dip angle is $20°$, and azimuth is $0°$. The x range of aerial survey line is $-400{\sim}400$ m, $y = 50$ m, $z = 50$ m, and the point distance is 50 m. The survey line in the borehole is $x = 30$ m, $y = 50$ m, the z range is $-400{\sim}0$ m, and the point distance is 10 m. The design model and survey line are shown in Figure 27.
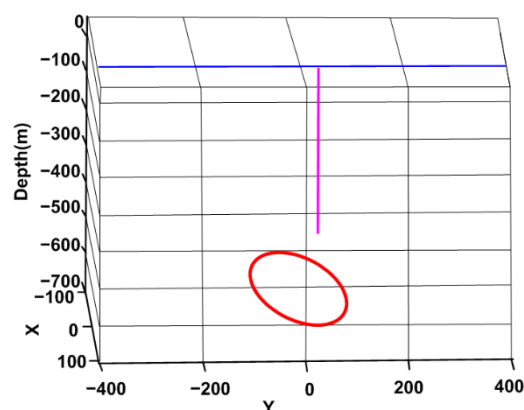

Figure 27. Model and survey lines.

The initial model is set as follows: the radius of the current loop is 150 m, the current is 150 mA, and the center point is located at $(0, 0, -450 \text{ m})$, the dip angle is $0°$, and the azimuth is $0°$. The change of fitting difference during fitting iteration is shown in Figure 28. At the end of the 60th iteration, the fitting difference is about 1.6%. At this time, the inversion

parameters are: the radius of current loop is 111.28, the current is 88.78 mA, the center point is (3.38, −1.70, −593.19), the azimuth is 358.82°, and the dip angle is 19.44°.
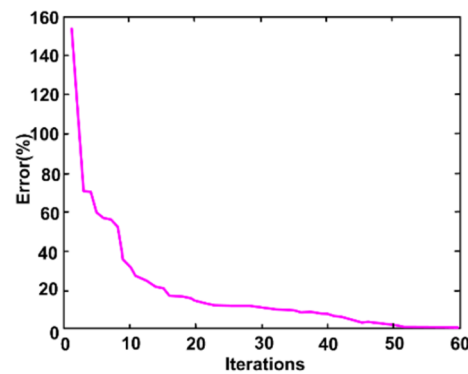

Figure 28. Fitting difference curve during iteration.

The shape of the inversion filament is shown in Figure 29, and is basically consistent with the design model. Figure 30 shows three component magnetic field response of the global minimum inversion model. Except for the radius and current parameters of the filament, the deviation of other parameters from the design parameters shall not exceed 5%. By studying the emission magnetic moment of the current loop, it can be found that the retrieved magnetic moment of the current loop is m ≈ 9879.45, and the deviation from the design magnetic moment is about 1.21%, which indicates that when the borehole data and air data are far away from the current loop, even if the borehole and air transient electromagnetic data are combined, there is still equivalence of the magnetic moment.
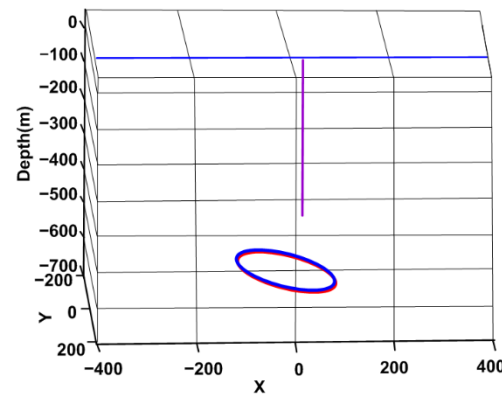

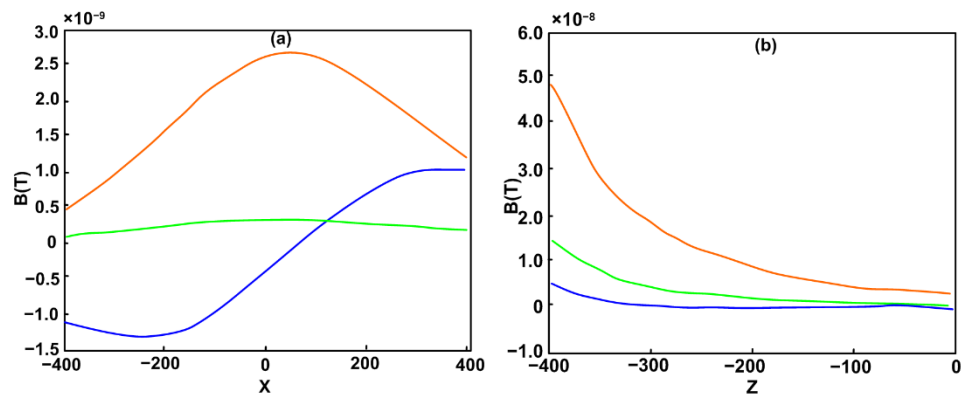**Figure 29.** Inversion current loop shape of global minimum.

Figure 30. Three component magnetic field response of global minimum inversion model (**a**) aerial response, (**b**) borehole response.

Only using aerial data for inversion, the relative fitting error after 60 iterations is 4.7%. At this time, the filament parameters are: the radius is 119.37, the current size is 76.45, the center point is (3.26, −38.64, −605.37), the azimuth is 334.26°, and the dip angle is 22.01°. Compared with the fitting results of the joint TEM data, the deviation between the inclination and the Y position of the center of the filament is larger when using the aerial data.

Only using borehole data for inversion, the relative fitting error after 60 iterations is 1.7%. At this time, the filament parameters are: the radius 110.27, current size 89.14, center point (7.56, −3.56, −586.44), the azimuth is 0° and the dip angle is 18.52°. Compared with the fitting results of joint data, the deviation between the parameters of filament retrieved from borehole data and the parameters of design filament is slightly larger, but smaller than that when only aerial data are used.

Results show that the parameters of the current loop can be recovered better when the air and well data are used together. In addition, compared with the case where the well passes through the current loop, this example has a large deviation for the radius of the current loop and the recovery of current parameters. The inversion method based on the current loop has strong magnetic moment equivalent effect when the well and air measuring points are far away from the current loop.

5.3. A Model with Two Abnormal Bodies

In order to verify the practicability of the inversion method in complex cases, a model of two conductive thin plates in free space is designed. The model parameters are as follows: Plate 1: the size of the plate 1 is 200 m × 200 m, the conductivity is 50 s, the coordinates of the center point is (−79.3, 0, −171), the dip angle is 45°, and the azimuth is 0°. Plate 2: the size of the plate 2 is 200 m × 200 m, the conductivity is 50 s, the coordinates of the center point are (150, 50, −500), the dip angle is 30°, and the azimuth is 180°, as shown in Figure 31.
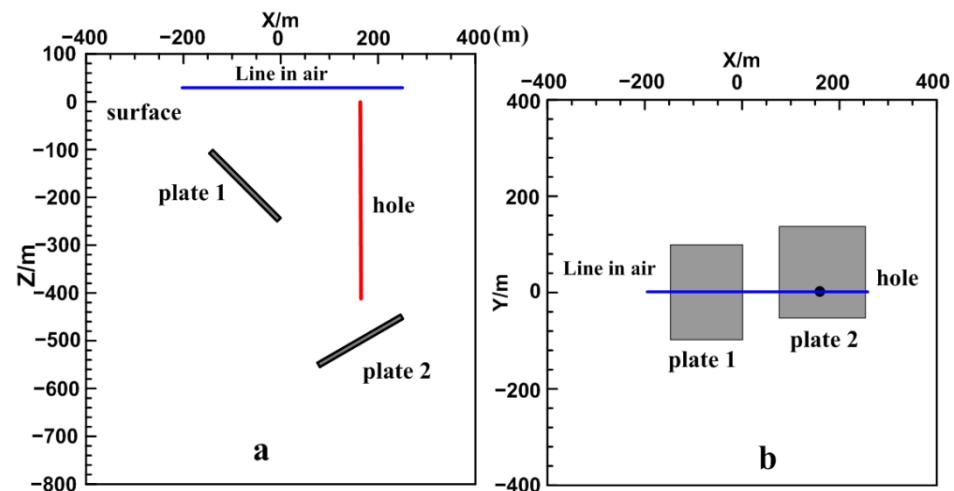

Figure 31. The diagram of the design model and survey lines. (**a**) Front view, (**b**) Top view.

Since there are two conductive plates in the model at the same time, two filaments are selected for inversion. Figure 32 shows the inversion results, showing the three component response curves of the aerial survey line and the survey points along the borehole. Figure 32c shows the comparison between the theoretical model and the inversion results. The inversion parameters of the two equivalent filaments in different time channels are given in Table 9. The results show that for the model with two conductors, even if the borehole does not pass through any conductor, the inversion using two equivalent current loops can still obtain reasonable results. Although the radius of the equivalent current loop in the inversion results deviates from the theoretical value, its center position, azimuth and dip angle are still relatively accurate.
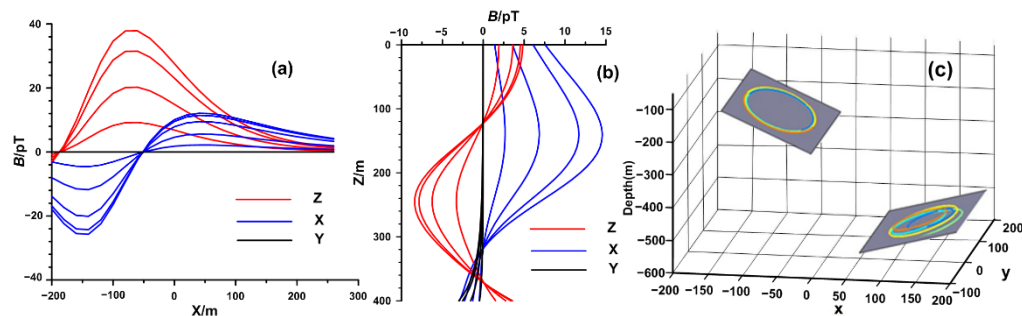
Figure 32. Inversion results. (**a**) three component response of aerial line, (**b**) three component response in borehole, (**c**) comparison of inversion results and theoretical results.

Table 9. Joint inversion results with borehole and aerial TEM data.

Filament No.	Chn	r (m)	I (mA)	x (m)	y (m)	z (m)	θ (°)	φ (°)
1	5	82.21	56.67	−80.62	−4.59	−168.00	43.83	353.04
1	10	80.85	47.00	−80.63	−4.84	−167.97	43.80	352.90
1	15	78.17	29.46	−80.95	−5.14	−168.11	43.82	352.71
1	20	77.15	8.14	−80.50	−5.29	−167.94	43.69	352.53
1	25	76.85	0.31	−80.25	−5.42	−167.70	43.58	352.51
2	5	58.51	57.22	111.28	44.64	−518.51	32.02	174.33
2	10	72.00	51.68	118.81	34.59	−516.82	33.09	183.19
2	15	71.71	15.36	127.79	32.21	−525.40	35.64	181.01
2	20	60.21	9.23	111.61	35.64	−521.69	33.43	178.42
2	25	53.46	0.73	128.89	35.95	−510.68	33.19	179.10

6. Conclusions

In this paper, a combined configuration of surface to borehole TEM and surface to air TEM is proposed, and an approximate joint inversion method based on equivalent filament is given. The results of the theoretical model calculation show that the approximate inversion method of the equivalent filament can be applied to the interpretation of high conductivity plates, and reliable results can still be obtained when 40% random noise is added. The inversion results using both borehole data and aerial data are more accurate than using borehole data or aerial data alone.

The analysis of the field of the equivalent filament affected by seven parameters shows that the aerial data are more sensitive to the vertical position of the filament, while the borehole data are more sensitive to the horizontal position, the azimuth, and dip angle of the filament.

The role of borehole data and aerial data may not be the same under different circumstances. Generally speaking, for the ore body close to the borehole or with a large, buried depth, the curve characteristics of the data in the borehole will be more obvious, while the requirements for the degree of curve fitting in the borehole are higher in the joint inversion. In this case, the data in the borehole will play a greater role in geometry recognition. However, when the ore body is far away from the borehole or the burial depth is very shallow, the aerial data can better reflect the characteristics of the abnormal body and play a more important role in inversion.

Author Contributions: Conceptualization: J.W. and Q.Z.; methodology: J.W., Q.Z., X.D., X.W. and Y.Y.; funding acquisition: All participants; writing—review and editing: J.W. and Q.Z.; All authors have read and agreed to the published version of the manuscript.

Data Availability Statement: Not applicable.

Conflicts of Interest: The authors declare no conflict of interest.

References

1. Barnett, C.T. Simple inversion of time-domain electromagnetic data. *Geophysics* **1984**, *49*, 925–933. [CrossRef]
2. Cull, J.P. Rotation and resolution of three-component DHEM data. *Explor. Geophys.* **1996**, *27*, 155–159. [CrossRef]
3. Polzer, B. The role of borehole EM in the discovery and definition of the Kelly Lake Ni-Cu deposit, Sudbury, Canada. In *SEG Technical Program Expanded Abstracts*; Society of Exploration Geophysicists: Houston, TX, USA, 2000; pp. 1063–1066.
4. Alan, K. Deep drill hole electromagnetic surveys for nickel/copper sulphides at Sudbury, Canada. *Explor. Geophys.* **1996**, *27*, 105–118.
5. Spicer, B. Geophysical signature of the Victoria property, vectoring toward deep mineralization in the Sudbury Basin. *Interpretation* **2016**, *4*, 281–290. [CrossRef]
6. Duncan, A.C. Interpretation of down-hole transient EM data using current filaments. *Explor. Geophys.* **1987**, *18*, 36–39. [CrossRef]
7. Fullagar, P.K. Inversion of Downhole TEM Data Using Circular Current Filaments. *Explor. Geophys.* **1987**, *18*, 341–344. [CrossRef]
8. Hughes, N.A.; Ravenhurst, W. Three component DHEM surveying at Balcooma. *Explor. Geophys.* **1996**, *27*, 77–89. [CrossRef]
9. Zhang, J.; Lv, G.Y.; Zhao, J.X.; Chen, X.D.; Zhao, Y. The Method of Surface-borehole TEM Vector Intersection and its Application. *Comput. Tech. Geophys. Geochem. Explor.* **2007**, *29*, 162–165.
10. Meng, Q.X.; Hu, X.Y.; Pan, H.P.; Zhou, F. Numerical analysis of multicomponent responses of surface-hole transient electromagnetic method. *Appl. Geophys.* **2017**, *14*, 175–186.
11. Adamson, M.; Ray, B.; Huizi, A. Using low frequency ground and downhole TDEM to explore for massive sulfide mineralisation in the Carajás mineral province. *ASEG Ext. Abstr.* **2019**, *2019*, 1–3. [CrossRef]
12. Zhang, Z.; Xiao, J. Inversions of surface and borehole data from large-loop transient electromagnetic system over a 1-D earth. *Geophysics* **2001**, *66*, 1090–1096. [CrossRef]
13. Liu, C. Study on 3D Forward Modeling & Inversion of Surface-Borehole Electromagnetic Data. Ph.D. Thesis, Université du Québec en Abitibi-Témiscamingue, Rouyn-Noranda, QC, Canada, 2021.
14. Yang, D.; Fournier, D.; Kang, S.; Oldenburg, D.W. Deep mineral exploration using multi-scale electromagnetic geophysics: The Lalor massive sulphide deposit case study. *Can. J. Earth Sci.* **2019**, *56*, 544–555. [CrossRef]
15. Eadie, T.; Staltari, G. Introduction to down hole electromagnetic methods. *Explor. Geophys.* **1987**, *18*, 247–351. [CrossRef]
16. Thomas, L. A simple Interpretation Aid for Downhole Time-Domain Electromagnetic Anomalies. *Explor. Geophys.* **1987**, *18*, 349–351. [CrossRef]
17. Wu, J.J.; Zhi, Q.Q.; Li, X.; Yang, Y.; Wang, X.C.; Zhang, J.; Deng, X.H. 3Dinversion method of fixed-loop TEM with three-component pure anomaly response. *Prog. Geophys.* **2015**, *30*, 2827–2835.
18. Wu, J.J.; Li, X.; Zhi, Q.Q.; Qi, Z.P.; Guo, J.L.; Deng, X.H.; Zhang, J.; Wang, X.C.; Yang, Y. Full field apparent resistivity definition of Borehole TEM with electrical source. *Chin. J. Geophys.* **2017**, *60*, 1595–1605.
19. Wu, J.J.; Li, X.; Zhi, Q.Q.; Qi, Z.P.; Guo, J.L.; Deng, X.H. Analysis of three component TEM response characteristic of electric source dill hole TEM. *Prog. Geophys.* **2017**, *32*, 1273–1278.
20. Elliott, P. New airborne electromagnetic Method Provides Fast Deep-target Data Turnaround. *Lead. Edge* **1996**, *15*, 309–310. [CrossRef]
21. Elliott, P. The Principles and Practice of FLAIRTEM. *Explor. Geophys.* **1998**, *29*, 58–60. [CrossRef]
22. Mogi, T.; Tanaka, Y.; Kusunoki, K.; Morikawa, T.; Jomori, N. Development of Grounded Electrical Source Airborne Transient EM (GREATEM). *Explor. Geophys.* **1998**, *29*, 61–64. [CrossRef]
23. Mogi, T.; Kusunoki, K.; Kaieda, H.; Ito, H.; Joromi, A.; Yuuki, Y. Grounded Electrical source Airborne Transient Electromagnetic (GREATEM) Survey of mount Bandai, North-eastern Japan. *Explor. Geophys.* **2009**, *40*, 1–7. [CrossRef]
24. Lin, J.; Xue, G.Q.; Li, X. Technological innovation of semi-airborne electromagnetic detection method. *Chin. J. Geophys.* **2021**, *64*, 2995–3004.
25. Ma, Z.J.; Di, Q.Y.; Lei, D.; Gao, Y.; Zhu, J.; Xue, G. The optimal survey area of the semi-airborne TEM method. *J. Appl. Geophys.* **2020**, *172*, 103884. [CrossRef]
26. Smirnova, M.; Becken, M.; Nittinger, C.; Yogeshwar, P.; Mörbe, W.; Rochlitz, R.; Steuer, A.; Costabel, S.; Smirnov, M.Y.; the DESMEX Working Group. A novel semi-airborne frequency-domain CSEM system.Three-dimensional inversion of semi-airborne data from the flight experiment over an ancient mining areanear Schleiz, Germany. *Geophysics* **2019**, *84*, E281–E292. [CrossRef]
27. Smith, R.S.; Annan, P.; McGowan, P.D. A Comparison of Data from Airborne, Semi-airborne, and Ground Electromagnetic Systems. *Geophysics* **2001**, *66*, 1379–1385. [CrossRef]
28. Yin, C.C.; Zhang, B.; Liu, Y.H.; Ren, X.Y.; Qi, Y.F.; Pei, Y.F.; Qiu, C.K.; Huang, X.; Huang, W.; Miao, J.J. Review on airborne EM technology and developments. *Chin. J. Geophys.* **2015**, *58*, 2637–2653.
29. Di, Q.Y.; Zhu, R.X.; Xue, G.Q.; Yin, C.C.; Li, X. New development of the Electromagnetic (EM) methods for deep exploration. *Chin. J. Geophys.* **2019**, *62*, 2128–2138.
30. Xue, G.Q.; Zhang, L.B.; Zhou, N.N.; Chen, W.Y. Developments measurements of TEM sounding in China. *Geol. J.* **2020**, *55*, 1636–1643. [CrossRef]

31. Li, X.; Hu, W.M.; Xue, G.Q. 3D modeling of multi-radiation source semi-airborne transient electromagnetic response. *Chin. J. Geophys.* **2021**, *64*, 716–723.

32. Li, X.; Zhang, Y.Y.; Lu, X.S.; Yao, W.H. Inverse Synthetic Aperture Imaging of Surface to airborne transient electromagnetic method with a galvanic source. *Chin. J. Geophys.* **2015**, *58*, 277–288.

33. Ji, Y.J.; Li, S.Y.; Yu, S.B.; Zhu, K.G.; Zhou, F.D.; Wang, Y.Z.; Wang, S.L.; Liu, H.J.; Ren, G.Q.; Lin, J. A study on time-domain AEM testing and calibration method based on anomaly loop. *Chin. J. Geophys.* **2011**, *54*, 2690–2697.

34. Zhi, Q.Q.; Wu, J.J.; Wang, X.C.; Yang, Y.; Zhang, J.; Deng, X.H. Three-component interpretation technique of fixed source TEM and its experimental application in metallic ore district. *Geophys. Geochem. Explor.* **2016**, *40*, 798–803.

35. Jiang, B.Y. *A Practical Near Zone Magnetic Source Transient Electromagnetic Exploration*; Geological Publishing House: Beijing, China, 1998.

36. Dyck, A.V. The role of simple computer models in interpretations of wide-band, drill-hole electromagnetic surveys in mineral exploration. *Geophysics* **1984**, *49*, 957. [CrossRef]

37. Nabighian, M.N. Quasi-static transient response of a conducting half-space—An approximate representation. *Geophysics* **1979**, *44*, 1700–1705. [CrossRef]